

Transient Two-Phase Flow in Slide-Gate Nozzle and Mold of Continuous Steel Slab Casting with and without Double-Ruler Electro-Magnetic Braking



SEONG-MOOK CHO, BRIAN G. THOMAS, and SEON-HYO KIM

Transient mold flow could produce undesirable surface instabilities and slag entrainments, leading to the formation of defects during continuous slab casting of steel. In this work, two Large Eddy Simulations coupled with Discrete Phase Model are run, with and without MagnetoHydroDynamic model, to gain new insights into the surface variations of molten steel-argon gas flow with anisotropic turbulence in the slide-gate nozzle and the mold, with and without double-ruler Electro-Magnetic Braking (EMBr). The model calculations are validated with plant measurements, and applied to investigate the flow variations related to the slide gate on nozzle swirl, jet wobbling, and surface flow variations by quantifying the variations of velocity, horizontal angle, and vertical angle of the transient flow. Transient flow in the slide-gate nozzle bottom is almost always swirling, alternating chaotically between clockwise and counter-clockwise rotation. The clockwise swirl, caused by stronger flow down the same side of the nozzle as the open area near the Outside Radius side of the slide-gate middle plate, produces faster jet flow and higher velocity flow across the top surface of the mold. Counter-clockwise swirl produces slower jet and surface flow, but with more variations. The double-ruler EMBr decreases the asymmetry and duration of velocity variations during nozzle swirl flipping, resulting in less flow variations in the jet and across the surface in the mold.

DOI: 10.1007/s11663-016-0752-4

© The Minerals, Metals & Materials Society and ASM International 2016

I. INTRODUCTION

TRANSIENT fluid flow phenomena in the mold during continuous casting of steel slabs are important to quality and defects in the final product. Abnormal surface flow is well known to aggravate meniscus-level fluctuations,^[1,2] shear instability of the molten slag/steel interface,^[3-5] and vortex formation^[6,7] near the Submerged Entry Nozzle (SEN), which leads to mold slag entrainment. The mold slag entrapped by the solidifying steel shell can cause both surface defects and internal defects. These defect-related flow phenomena in the mold become more complex with argon gas, which is injected into the nozzle to prevent the nozzle clogging. Increasing argon gas volume fraction^[8] or decreasing bubble size^[9] can cause the jet to bend more upward, and even change the mold flow pattern from a

double-roll pattern to a single-roll pattern. In addition to changing the mold flow pattern, argon gas also increases surface turbulence^[10] with long-term asymmetry and unbalanced transient flow in the lower recirculation region, causing bubbles to penetrate deeply.^[11,12]

To stabilize and optimize the transient fluid flow in the mold, ElectroMagnetic (EM) systems are often applied, especially at high casting speed. Many researchers have previously investigated the effect of EMBr on single-phase (molten steel) flow of molten steel.^[13-22] Cukierski and Thomas investigated the average effect of local EMBr on steady-state flow in the mold by applying standard $k-\epsilon$ model and plant measurements.^[16] Chaudhary *et al.*^[20] and Singh *et al.*^[21] performed Large Eddy Simulation (LES) of the GaInSn physical model adopted by Timmel *et al.*,^[17,18] to quantify the effect of ruler EMBr on transient mold flow pattern in the mold, having different wall conductivity; insulated and conducting walls. Some previous studies have considered the effect of EMBr on time-averaged two-phase (molten steel-argon) flow in the mold.^[23-29] The molten steel-argon jet flowing from the SEN deflects around the strongest region of the magnetic field, resulting in nonuniform flow under some conditions.^[29]

Double-ruler EMBr employs two static magnetic fields across the mold width: one ruler above the nozzle ports to stabilize the flow uprising towards the top surface and a second ruler added below the jets to deflect the jets upwards and to decrease the downward flow penetration. Li *et al.* studied the effect of double-ruler EMBr with argon gas injection on mold flow^[23] and

SEONG-MOOK CHO, Postdoctoral Research Associate, is with the Department of Mechanical Science and Engineering, University of Illinois at Urbana-Champaign, 1206 West Green Street, Urbana, IL 61801. BRIAN G. THOMAS, Professor, is with the Department of Mechanical Engineering, Colorado School of Mines, 1500 Illinois Street, Golden, Colorado 80401, and is also C. J. Gauthier Professor Emeritus and Research Professor, University of Illinois at Urbana-Champaign, 1206 West Green Street, Urbana, IL 61801 Contact e-mail: bgthomas@illinois.edu SEON-HYO KIM, Professor, is with the Department of Materials Science & Engineering, Pohang University of Science & Technology, 77 Cheongam-Ro, Nam-Gu, Pohang, Gyeongbuk 790-784, Republic of Korea.

Manuscript submitted March 20, 2016.

Article published online July 14, 2016.

biased flow induced by nozzle misalignment.^[24] However, only a few previous studies have quantified the EMBR effect on transient two-phase (molten steel-argon gas) fluid flow.^[30] Cho *et al.* used nail board dipping tests and eddy-current sensor monitoring to visualize and quantify the variations of surface velocity and surface level during nominally steady slab casting with slide-gate flow control. They found that double-ruler EMBR is effective at decreasing velocity fluctuations, with little effect on average surface velocity in the mold.^[30]

In the present work, LES coupled with Discrete Phase Modeling (DPM) is applied to quantify transient behavior of molten steel-argon gas flow in the slide-gate nozzle and mold with and without double-ruler EMBR during nominally steady continuous slab casting of steels. Instantaneous and time-averaged flow patterns in both the nozzle and mold are quantified, including variations of velocity histories in the jet and top surface, to investigate the relation between nozzle flow and mold flow variations with and without the EMBR. Further insight into the transient flow variations is quantified by analyzing histories of vertical and horizontal angles of the predicted transient flow in the nozzle and mold. Finally, for model validation, the predicted surface velocity and surface level were compared with the previous plant measurements.^[31]

II. COMPUTATIONAL MODEL

A three-dimensional finite-volume model employing LES was applied to calculate transient flow of molten steel and argon gas in the nozzle and mold with and without double-ruler EMBR. Starting from the steady-state single-phase flow field calculated with a Reynolds Averaged Navier–Stokes (RANS) model using the standard $k-\epsilon$ model,^[32] the LES coupled with the DPM was run to calculate the transient two-phase flow, considering the interaction between the molten steel flow and argon bubble motion. Then, the effect of the static magnetic field of the double-ruler EMBR on the two-phase flow was simulated by including the magnetic induction MagnetoHydroDynamic (MHD) equations. These models were implemented into the commercial package ANSYS FLUENT.^[33] Details of the models are summarized below.

A. Governing Equations for LES with DPM and MHD Models

Mass conservation of the molten steel is as follows

$$\frac{\partial}{\partial x_i}(\rho u_i) = S_{\text{shell,mass}}, \quad [1]$$

where ρ is molten steel density, u_i is velocity in the three coordinate directions, and $S_{\text{shell,mass}}$ is a mass sink term to account for solidification of the molten steel.^[34–36] This sink term is applied in those fluid cells on the wide faces and the narrow faces next to the interface between the fluid zone of the molten steel and the solid zone of the steel shell.

The time-dependent momentum balance equations for molten steel affected by argon gas motion and electromagnetic force are as follows

$$\begin{aligned} \frac{\partial}{\partial t}(\rho u_i) + \frac{\partial}{\partial x_j}(\rho u_i u_j) = & -\frac{\partial p^*}{\partial x_i} + \frac{\partial}{\partial x_j} \left[(\mu + \mu_t) \left(\frac{\partial u_i}{\partial x_j} + \frac{\partial u_j}{\partial x_i} \right) \right] \\ & + S_{\text{shell,mom},i} + S_{\text{Ar,mom},i} + F_{L,i} \end{aligned} \quad [2]$$

p^* is modified pressure ($p^* = p + \frac{2}{3}\rho k_r$), p is gage pressure, k_r is residual kinetic energy, μ is dynamic viscosity of molten steel, μ_t is turbulent viscosity and modeled with the Wall-Adapting Local Eddy (WALE) subgrid-scale viscosity model,^[33,37] to account for turbulent eddies that are too small to be resolved by the mesh. $S_{\text{shell,mom},i}$ is a momentum sink term in each component direction to consider solidification of the molten steel on the wide faces and the narrow faces.^[34–36] This term is applied to the cells with $S_{\text{shell,mass}}$. $S_{\text{Ar,mom},i}$ is a momentum source term to incorporate the effect of argon gas bubble motion on the molten steel flow. This term is calculated using the Lagrangian DPM model, which solves a force balance including the drag, buoyancy, virtual mass, and pressure gradient forces that act on each argon bubble. Details of the DPM equations are given elsewhere.^[32,33] $F_{L,i}$ is a Lorentz force source term to include the effect of the applied magnetic field on the two-phase flow field. This source term is calculated by considering the interaction among the flow field, the induced current density, and the total magnetic field. The total magnetic field includes the measured external magnetic field and the induced magnetic field, which is calculated with the magnetic induction equation.^[31,38]

To quantify the fluctuations of velocities in each three coordinate direction from the LES model results, root mean square (RMS) of velocity fluctuations $\sqrt{(u'_i)^2}$ are calculated as follows:

$$\sqrt{(u'_i)^2} = \sqrt{\frac{1}{n} \sum_{t=0}^n (u_{i,t} - \bar{u}_{i,t})^2}, \quad [3]$$

where i is the coordinate (x , y , and z), t is time step, and n is the total number of time steps in the time-averaging period.

For further understanding of flow instability, Turbulent Kinetic Energy (TKE) is obtained from the RMS velocity fluctuation components as follows:

$$\text{TKE} = \frac{\left[\sqrt{(u'_x)^2} \right]^2 + \left[\sqrt{(u'_y)^2} \right]^2 + \left[\sqrt{(u'_z)^2} \right]^2}{2} \quad [4]$$

B. Computational Domain and Mesh

The present work investigates a slide-gate system which controls the molten steel flow rate by moving a middle plate between the Outside Radius (OR) and Inside Radius (IR) as shown in Figure 1. To consider

the asymmetry between OR and IR sides with assuming symmetry between Narrow Faces (NFs), the computational model domain consists of the entire south (right) side half of the caster, including part of the bottom of the tundish, the Upper Tundish Nozzle (UTN), the slide gate, the SEN with typical bifurcated ports, and the top 3000 mm of the molten steel pool and solid steel shell in the mold and strand. Details of the caster dimensions and computational domain are included in Table I. The steel shell thickness profile is given by $S = k\sqrt{t}$, where S (mm) is steel shell thickness, t (seconds) is time for the shell to travel from the meniscus, and constant k is 2.94 mm/s^{0.5}, according to the measured thickness profile of a break-out shell from this caster.^[32] This domain consists of ~1.8 million hexahedral cells as shown in Figure 2.

C. Boundary Conditions

In the LES, constant velocity was fixed as the inlet condition at the outside surface of the tundish bottom region. This velocity V_{inlet} (0.00938 m/s) was calculated according to the molten steel flow rate Q_{inlet} (0.00921 m³/s) and the surface area A_{inlet} (0.982 m²) of the circular top and cylindrical sides of the tundish bottom region ($V_{inlet} = Q_{inlet}/A_{inlet}$). A pressure outlet condition of 0 Pa (gauge) was chosen on the domain bottom boundary (strand exit). The interfaces between the molten steel fluid flow region and the steel shell boundary were no-slip walls ($u_x = u_y = u_z = 0$). The top surface (interface with the slag layers) was also considered as a no-slip wall, due to the high slag viscosity.

For the DPM model calculation, argon gas volume fraction of 5.6 pct (based on 16.5 LPM in each domain half with temperature 1827 K (1554 °C) and pressure 1.87 atm, estimated at the UTN) was injected through the inner-wall surface area of the UTN refractory with a uniform bubble size of 0.81 mm. This diameter was estimated from a two-stage (expansion and elongation) analytical model of bubble formation^[39] coupled with an empirical model of active sites of bubble formation.^[40] An escape condition was adopted at the domain bottom exit and at the top surface.^[33] A reflection condition was employed at other walls.

For the MHD model, a realistic treatment was considered by including the conducting steel shell in the domain as a solid zone for the calculation of current flow. The exterior boundary, where the shell is surrounded by the nonconducting slag layer, was electrically insulated.

D. Numerical Details

In the LES model, the three equations for the three momentum components (bounded central differencing) and the pressure Poisson equation (standard) were discretized using the finite-volume method in ANSYS FLUENT 14.5.^[33] The mass and momentum sink terms, $S_{shell,mass}$ and $S_{shell,mom,i}$, were implemented with user-defined functions (UDF). The discretized equations were solved for velocity and pressure by the Semi-Implicit Pressure Linked Equations (SIMPLE) algorithm, starting with an initial value of the steady-state single-phase flow field^[31] calculated by the standard $k-\epsilon$ model. The LES with the Lagrangian DPM calculated

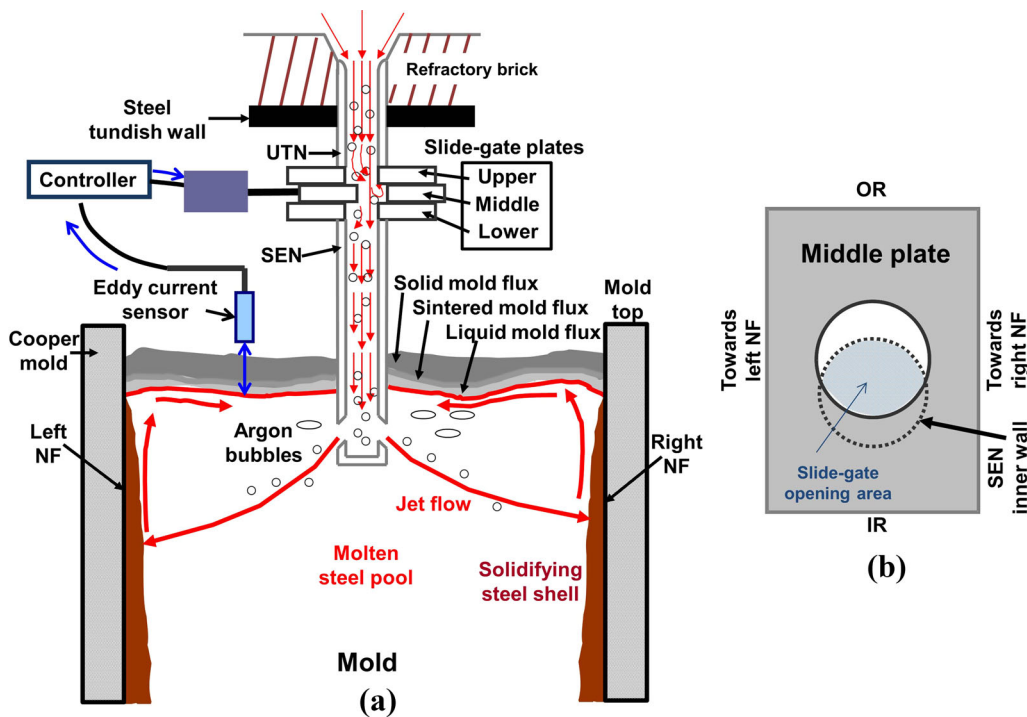


Fig. 1—(a) Schematic of slide gate in continuous slab casting of steel^[31] and (b) slide-gate middle plate on SEN.^[32]

Table I. Caster Dimensions and Process Conditions^[32]

Caster Dimensions	
Nozzle bore inner diameter	90 mm (at UTN top) to 80 mm (at bottom well)
Nozzle bore outer diameter	160 mm (at UTN top) to 140 mm (at SEN bottom)
Nozzle bottom well depth	19 mm
Nozzle port area	80 mm (width) × 85 mm (height)
Nozzle port angle	35 deg down (both top and bottom)
Distance from end of slide-gate middle plate to upper junction of nozzle port	840 mm
Mold thickness	250 mm
Mold width	1300 mm
Domain length	4648 mm (total); 3000 mm (strand region)
Process Conditions	
Steel flow rate	552.5 LPM (3.9 ton/min)
Casting speed	1.70 m/min (28.3 mm/sec)
Slide-gate opening ratio	84 pct
Argon gas flow rate (cold)	9.2 SLPM (1 atm, 273 K (0°C));
Argon gas flow rate (hot)	33.0 LPM (1.87 atm, 1827 K (1554°C))
Argon volume fraction	5.6 pct (hot)
Submerged depth of nozzle	164 mm
Meniscus level below mold top	103 mm
EMBr current (upper coil)	300 A (DC)
EMBr current (lower coil)	300 A (DC)

three momentum components and pressure on a structured mesh of ~1.8 million hexahedral cells, including the effect of the 592 argon bubbles injected through the UTN inner-wall surface every 0.0006 seconds time step.

The transient two-phase LES model without EMBr was started at time = 0 second and run for ~118.1 seconds. The first case of flow without EMBr was allowed to develop for ~15 seconds, and then a further ~103.1 seconds of data were used for compiling time-average results. The second case with EMBr was run by imposing the magnetic field by implementing the MHD equations into the LES coupled with DPM, starting with the flow field without EMBr at 30.3 seconds. This case of two-phase flow with EMBr was allowed to develop for ~10 seconds beyond ~30.3 seconds, and then a further ~98.5 seconds of data were obtained for time averaging. Each simulation required ~48 hours of wall-clock time to calculate 1 second of flow time in a parallel supercomputing using two nodes (total 32 cores) on Blue Waters at the National Center for Supercomputing Applications at the University of Illinois.

III. DOUBLE-RULER EMBR FIELD

The double-ruler EMBR applies an external magnetic field using Direct Current (DC) to the mold region in two ruler-shaped regions: upper ruler (300 A) and lower ruler (300 A). The magnetic field imposed by the EMBr was measured using a Gauss meter at 69 data points in the mold cavity without molten steel. On each of three vertical lines (parallel with casting direction), located 0, 350, and 700 mm from the mold center, 23 positions are measured by lowering the Gauss meter downward from the mold top to below 1100 with 50 mm increments.

Then, the measured field was extrapolated to cover the entire nozzle mold, and strand regions as given in Reference 31.

The full three-dimensional external magnetic field distribution, including the nozzle region and deep into the strand, is visualized in Figure 3. The field contours reveal two high peaks of ~0.17 T (solid line) imposed near the mold center: one just above the nozzle ports (~250 mm below mold top) and the other below the nozzle ports (~750 mm below mold top). These peaks decrease significantly towards the NF, where the imposed field strength is ~0.13 T (dash line). The effect of this field on the transport equations for the case of transient two-phase flow with EMBr was implemented using the magnetic induction MHD model.

IV. SWIRL FLOW IN SLIDE-GATE NOZZLE

A. Nozzle Internal Flow

Instantaneous and time-averaged flow patterns in the slide-gate nozzle are shown in Figure 4 at the center-middle plane between IR and OR (front view), and between left and right NFs (side view). Transient flow in the nozzle well-bottom region is almost always swirling (98 pct of the total time without EMBr, 94 pct with EMBr). The swirl direction alternates chaotically between clockwise rotation (*e.g.*, frames at 73.2 and 42.3 seconds) and counter-clockwise rotation (*e.g.*, frames at 87.0 and 67.5 seconds), persisting for 5 to 30 seconds time intervals before flipping directions. While flipping directions of the nozzle swirl, generally symmetric flow is observed for only 0.6 to 2.3 seconds (*e.g.*, frames at 81.6 and 53.7 seconds). These short durations show that symmetrical flow is rare and unstable. These

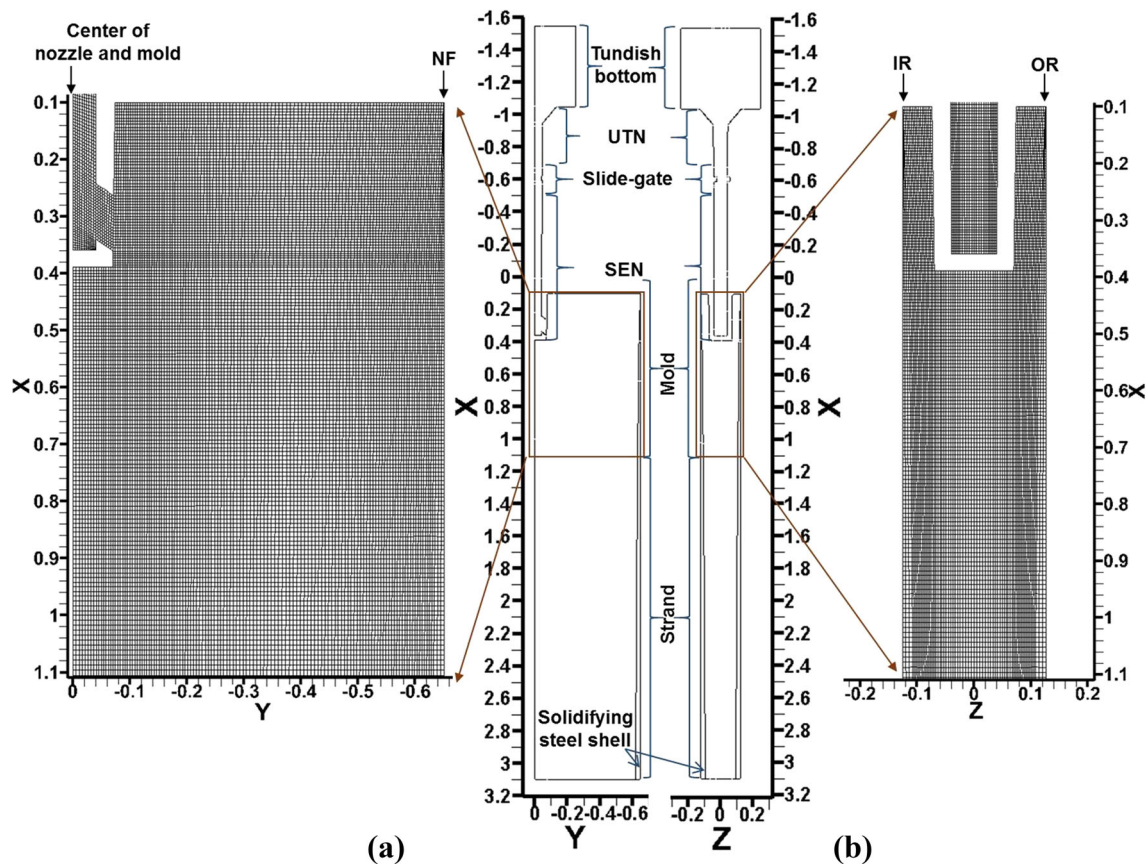


Fig. 2—Domain and mesh at center-middle planes (a) between IR and OR and (b) between right NF and left NF in the mold.

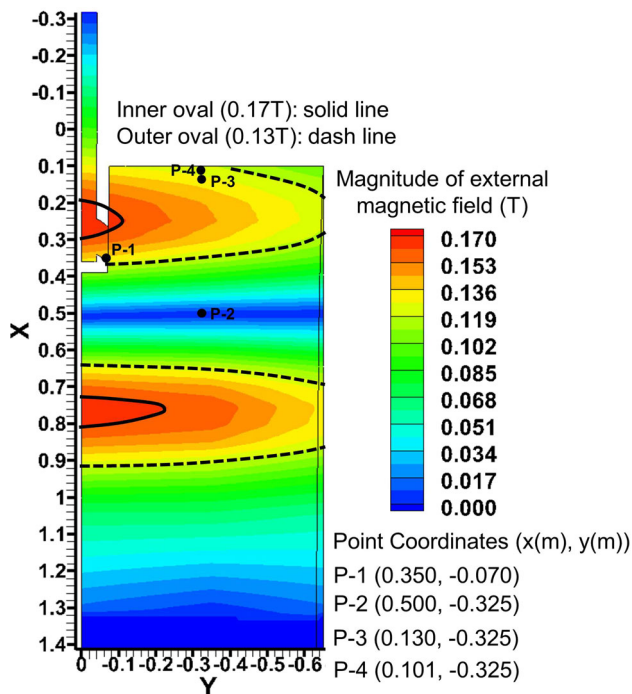


Fig. 3—Double-ruler EMBr magnetic field and location of points at the center-middle plane (between IR and OR) in the mold.

predicted nozzle swirl phenomena match closely with previous observations looking into the nozzle ports of water models.^[41,42]

The origin of the swirl is the asymmetric turbulent flow through the open area near the OR side of the middle plate of the slide gate at the top of the SEN. The high-momentum turbulent flow is stronger down the OR side of this SEN. When this persists all the way down the SEN, this generates a single, large, rotating eddy or “swirl” within the bottom region which is naturally clockwise. Usually, however, the flow crosses to impinge and become stronger down the IR side of the SEN. This generates counter-clockwise swirl, which predominates 63.9 pct of the time without EMBr, as shown in Table II. With EMBr, the upper ruler magnetic field extends upwards to induce strong magnetic forces across the SEN, which decrease the asymmetric flow down the SEN, resulting in less swirl momentum, smaller swirl size, and lower swirl velocities at the nozzle bottom. Furthermore, the EMBr tends to make the periods of the clockwise and counter-clockwise swirls more similar: counter-clockwise is encountered 53 pct of the time. In addition, the transition period of generally symmetrical flow increases from 2 pct without EMBr to 6 pct with EMBr. Thus, EMBr produces a more symmetrical time-averaged flow pattern with more changes in swirl direction (3 flips in 103.1 seconds without EMBr; 5 flips

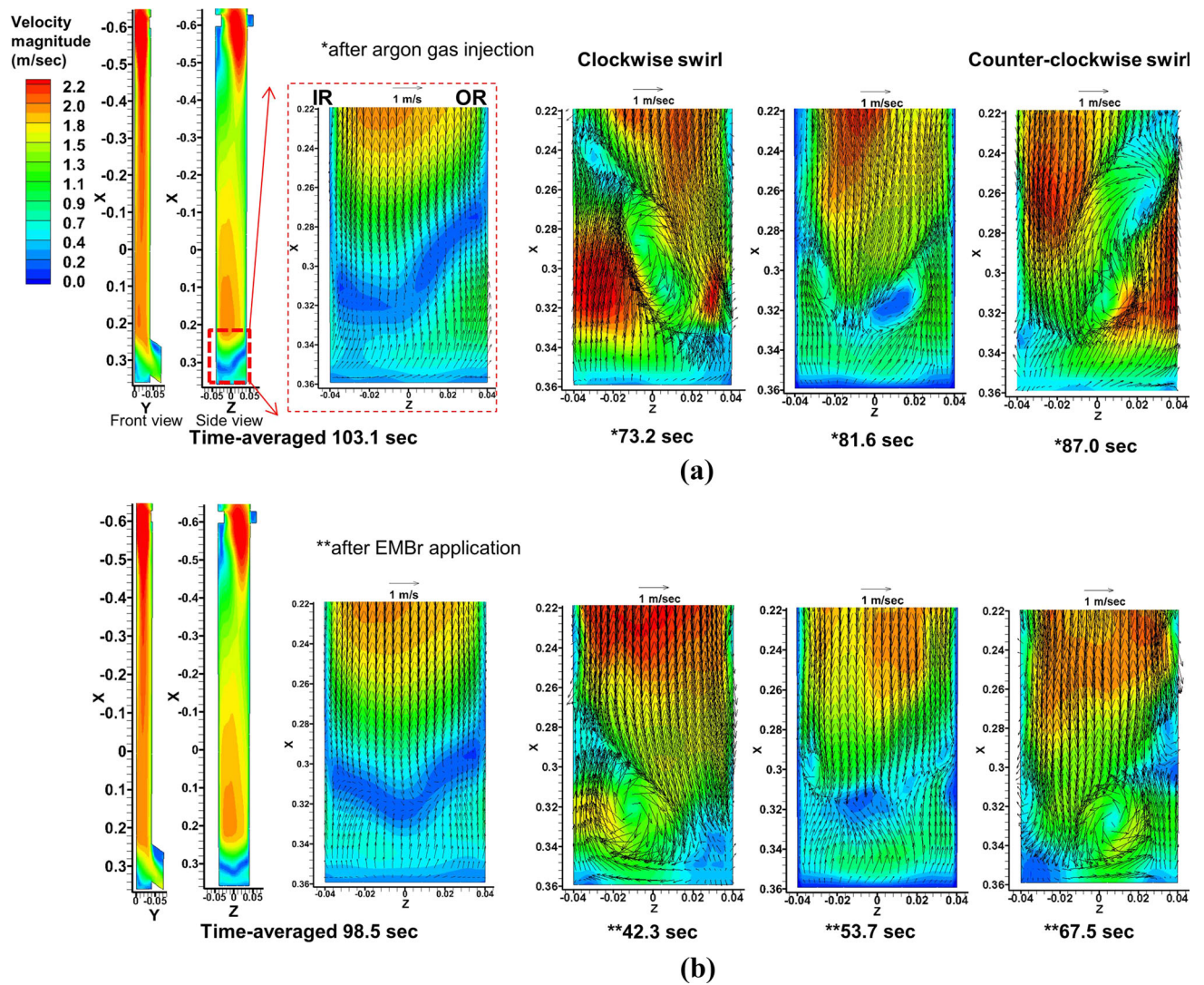


Fig. 4—Time-averaged and three instantaneous flow patterns in the nozzle inner region (a) without EMBR and (b) with EMBR.

Table II. Duration of Nozzle Swirl Flow Patterns

	Clockwise	Counter-Clockwise	Symmetric (Transition Period)	Total Time
Without EMBR	35.34 s (34.3 pct)	65.86 s (63.9 pct)	1.90 s (1.8 pct)	103.1 s
With EMBR	40.02 s (40.6 pct)	52.22 s (53.0 pct)	6.26 s (6.4 pct)	98.5 s

in 98.5 seconds with EMBR) at the nozzle bottom. Consequently, EMBR makes the flow more symmetrical at the nozzle port exit, as shown in the next section.

B. Port Outflow

Instantaneous and time-averaged flow patterns at the nozzle port exit are shown in Figure 5, with and without EMBR. Asymmetry between the IR and the OR sides of the port are observed at the nozzle port exit, due to the transient nozzle swirl. Clockwise swirl makes the jet flow more towards the OR side, both with and without EMBR (e.g., frames at 73.2 and 42.3 seconds). On the other hand, the jet exits the port nearer to the IR side

with counter-clockwise swirl (e.g., frames at 87.0 and 67.5 seconds). EMBR causes less asymmetry, as indicated in the peak time-average flow closer to point P-1 at the bottom center of the port (Figure 5 with EMBR) relative to the time-averaged flow without EMBR, where flow across the bottom of the nozzle port is shown to be stronger towards the IR side.

To further quantify the nozzle port flow, velocity magnitude histories are presented in Figure 6. This figure also shows the periods when the swirl direction is clockwise, counter-clockwise, or transitioning between these two flow regimes. The shaded regions show the periods of stable counter-clockwise flow (not including transition periods). Clockwise swirl produces slightly

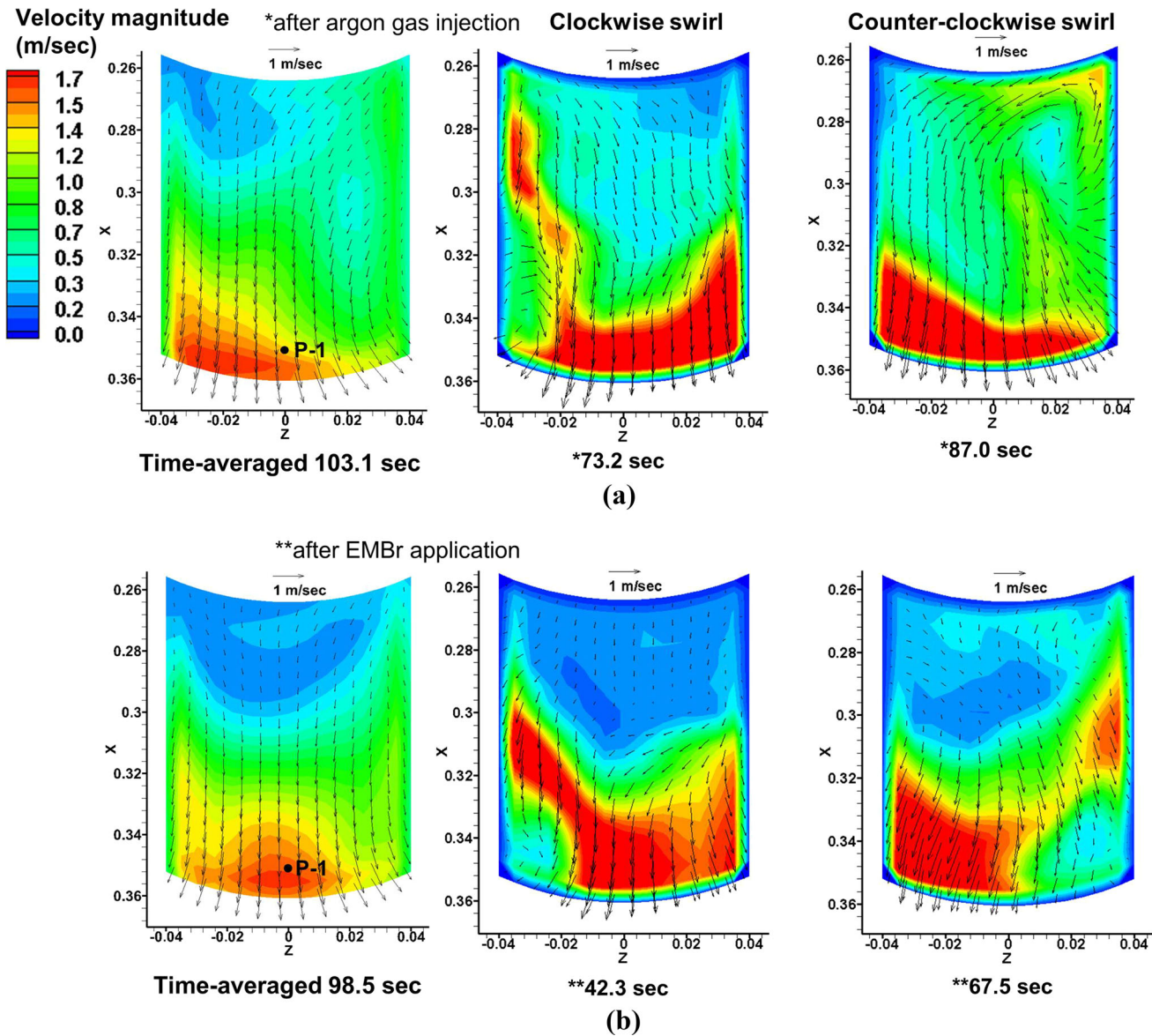


Fig. 5—Time-averaged and instantaneous flow patterns at the nozzle port (a) without and (b) with EMB.

higher time-averaged velocity magnitudes exiting the port, with smaller fluctuations than does counter-clockwise swirl, both with and without EMB. This important finding is quantified with time averages in Table III. This phenomenon is likely because the strong flow down the SEN OR wall that causes clockwise swirl has a shorter path from the slide gate to the nozzle bottom, resulting in less-momentum loss than experienced by the cross-over flow that causes counter-clockwise swirl. This is responsible for the asymmetry of velocity magnitude between clockwise and counter-clockwise swirl, given in Table III. EMB decreases the difference in velocity magnitude at point P-1 between clockwise and counter-clockwise swirl by ~33.3 pct: from 0.24 m/s (1.61 to 1.37 m/s) without EMB; to 0.16 m/s (1.71 to 1.55 m/s) with EMB. Because the jet core is more centered in the bottom at the nozzle port with EMB, velocity

magnitude is slightly higher. In addition, EMB decreases the velocity magnitude fluctuations at P-1 that accompany swirl direction flipping. The next section investigates the effect of these nozzle phenomena on flow in the mold.

V. MOLD FLOW VARIATIONS

Time-averaged and instantaneous flow patterns at the center-middle plane between the IR and OR in the mold are shown in Figure 7, with and without EMB. Without EMB, the time-averaged flow patterns exhibit a classic double-roll pattern. The streamlines show stable recirculation in the upper roll, but the lower roll is not fully developed, indicating that low-frequency variations (with periods longer than the time-averaging

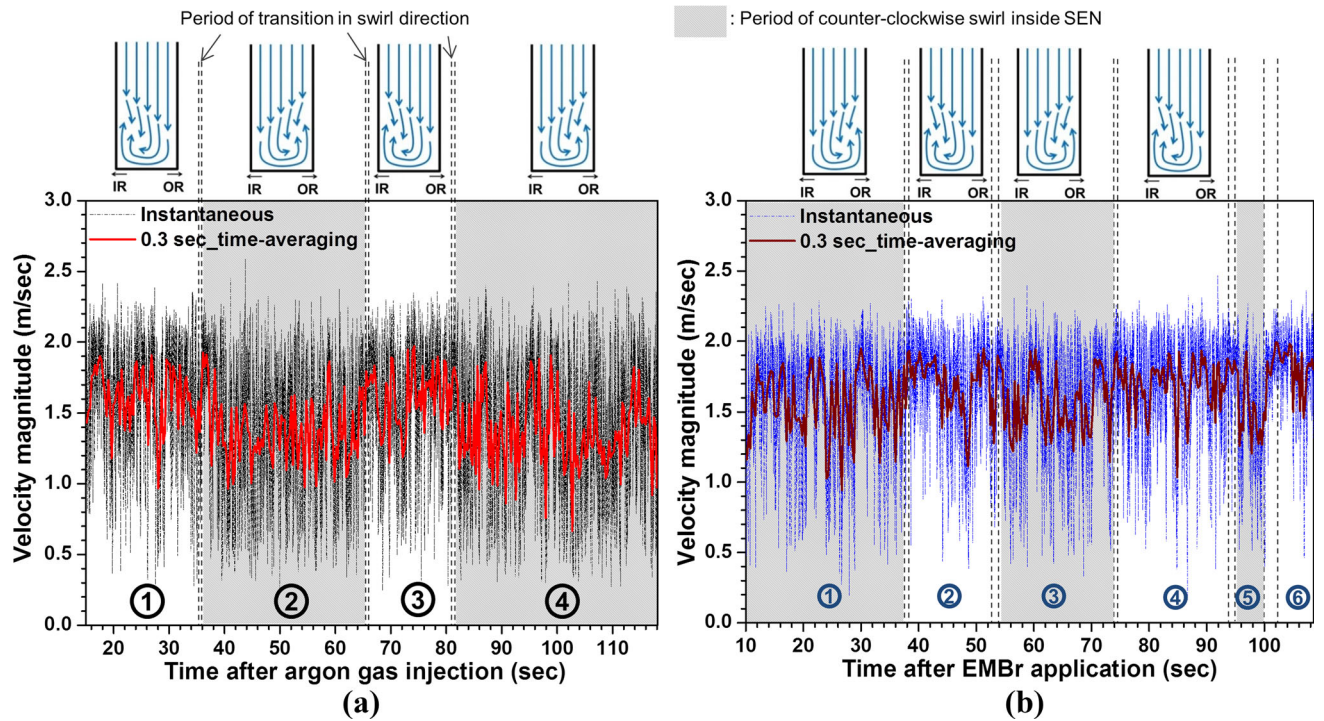


Fig. 6—Histories of velocity magnitude at P-1 (nozzle port) (a) without and (b) with EMBr.

Table III. Time-Averaged Velocity Magnitude at P-1 at Nozzle Port Exit

	Clockwise	Counter-Clockwise	Total Time
Without EMBr	1.61 ± 0.41 m/s	1.37 ± 0.47 m/s	1.46 ± 0.46 m/s
With EMBr	1.71 ± 0.34 m/s	1.55 ± 0.40 m/s	1.63 ± 0.38 m/s

window of 103.1 seconds) predominate there. Fast development of the upper-roll flow pattern with relatively high-frequency variations is promoted by the short residence time that accompanies its small size.

Application of the double-ruler EMBr changes this flow pattern somewhat. With EMBr, the lower roll develops faster, and its center eye moves closer to the jet. The jet is located in a region of relatively low magnetic field strength between the upper and lower rulers. Thus, the jet shape is only slightly thinner, and the vertical jet angle is deflected upwards slightly (from 27.4 deg down without EMBr to 24.6 deg down with EMBr, see Table IV). In addition, EMBr tends to stabilize a small roll that forms near the top surface near the SEN, due to the upward-rising argon bubbles in that region.

A. Jet Wobbling

Instantaneous mold flow patterns show up-and-down wobbling of the jet in the mold, which produces different impingement points on the NF. When the swirl exiting the port is clockwise, the accompanying faster jet bends upwards, impinging the NF horizontally, and produces very strong surface flow, as shown for example in Figure 7, in frames at 19.9 seconds without EMBr and at 42.2 seconds with EMBr. With counter-clockwise

swirl, the accompanying slower jet wobbles downwards to impinge at a lower position on the NF wall, and produces slower surface velocities (see frames at 63.3 and 68.0 seconds).

EMBr reduces the up-and-down jet wobbling in the mold, resulting in less surface flow variations. Thus, EMBr decreases the RMS of u_x (casting direction velocity) fluctuations, as shown in Figure 8, especially in the upper recirculation region. This corresponds to lower TKE.

Figure 9 shows time variations of velocity magnitude at point P-2 inside the jet in the mold. To consider the average lag time of 0.3 seconds from P-1 (nozzle port exit) to P-2, vertical red lines are drawn in this figure at the end of the transition in swirl direction from clockwise to counter-clockwise and at the start of the swirl direction transition from counter-clockwise to clockwise. Thus, each time period shaded between two red lines indicates when jet flow is expected to be affected by stable counter-clockwise swirl exiting the nozzle. Clockwise swirl from the nozzle port exit produces stronger jet flow, resulting in higher jet velocity magnitude, both with and without EMBr. Specifically, average velocity magnitude in the jet flow with clockwise swirl (0.59 m/s) is ~37 pct higher than with counter-clockwise swirl (0.43 m/s), without EMBr, as shown in

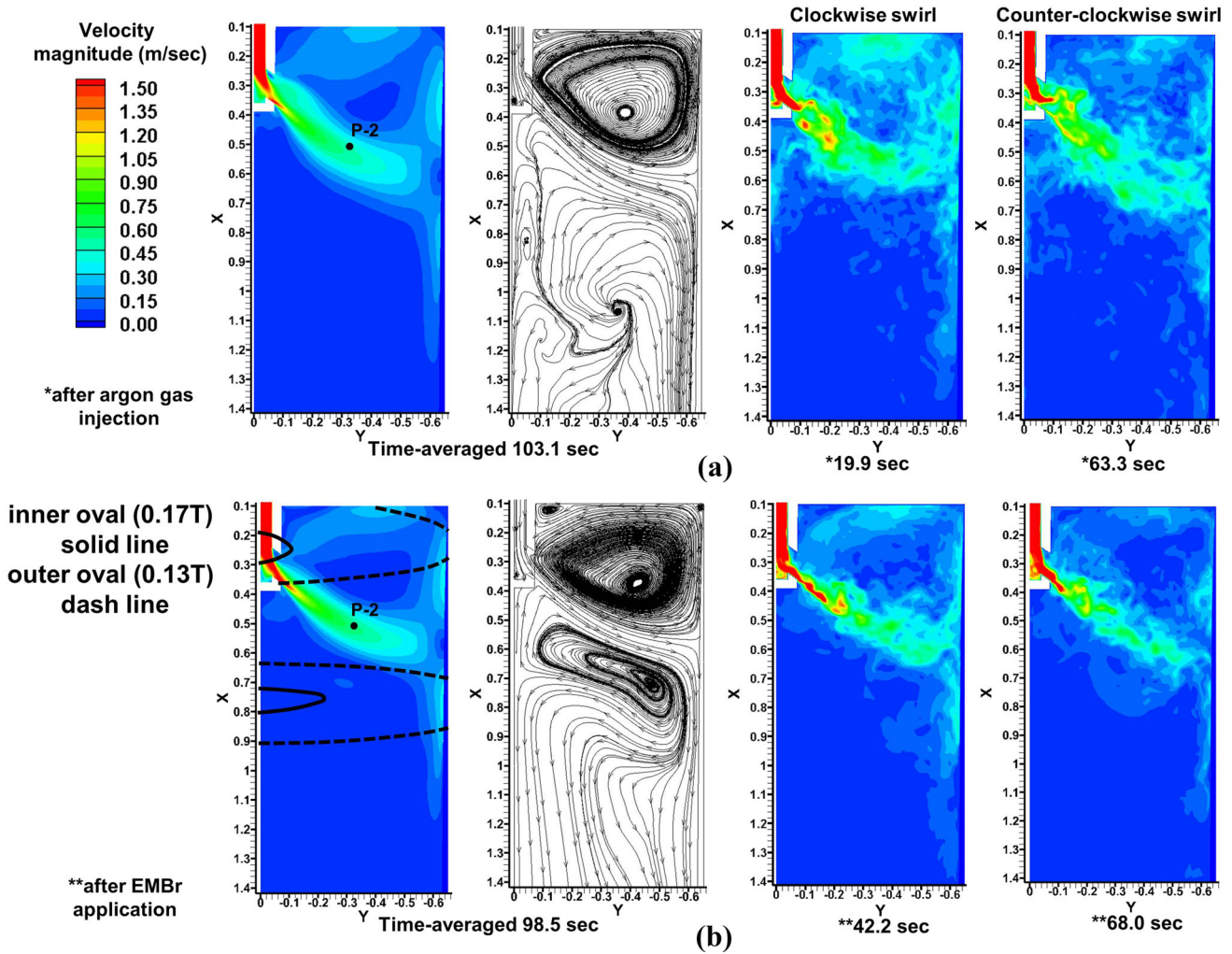


Fig. 7—Time-averaged and instantaneous flow patterns at the center-middle plane (between IR and OR) in the mold (a) without and (b) with EMBR.

Table IV. Jet Characteristics at P-2 in the Mold

	Clockwise	Counter-Clockwise	Total Time
Without EMBR			
Velocity magnitude	0.59 ± 0.18 m/s	0.43 ± 0.19 m/s	0.49 ± 0.20 m/s
Horizontal angle	1.59 ± 17.22 deg	-5.63 ± 29.73 deg	-3.01 ± 26.13 deg
Vertical angle	26.69 ± 16.45 deg	27.88 ± 27.64 deg	27.40 ± 24.19 deg
With EMBR			
Velocity magnitude	0.63 ± 0.17 m/s	0.54 ± 0.19 m/s	0.58 ± 0.19 m/s
Horizontal angle	2.70 ± 18.10 deg	-4.87 ± 21.59 deg	-1.66 ± 20.55 deg
Vertical angle	24.36 ± 15.23 deg	24.66 ± 18.31 deg	24.61 ± 17.01 deg

Table IV. The same trend is found with EMBR, but the velocity increase is only ~17 pct.

To further quantify these flow variations, histories of vertical angle $\theta_{\text{vertical},t}$ and horizontal angle $\theta_{\text{horizontal},t}$ of the jet were calculated at point P-2 as follows, and presented in Figures 10 and 11, respectively.

$$\theta_{\text{vertical},t} = -\tan^{-1}\left(\frac{u_{x,t}}{u_{y,t}}\right) \quad [5]$$

$$\theta_{\text{horizontal},t} = -\tan^{-1}\left(\frac{u_{z,t}}{u_{y,t}}\right), \quad [6]$$

where $u_{x,t}$, $u_{y,t}$, $u_{z,t}$ are instantaneous velocity components (at time t) in each coordinate direction. Details of the flow characteristics including velocity magnitude, horizontal angle, and vertical angle at point P-2 of the nozzle port are given in Table IV.

As shown in Figure 10, strong jet flow with higher velocity magnitude caused by clockwise swirl produces

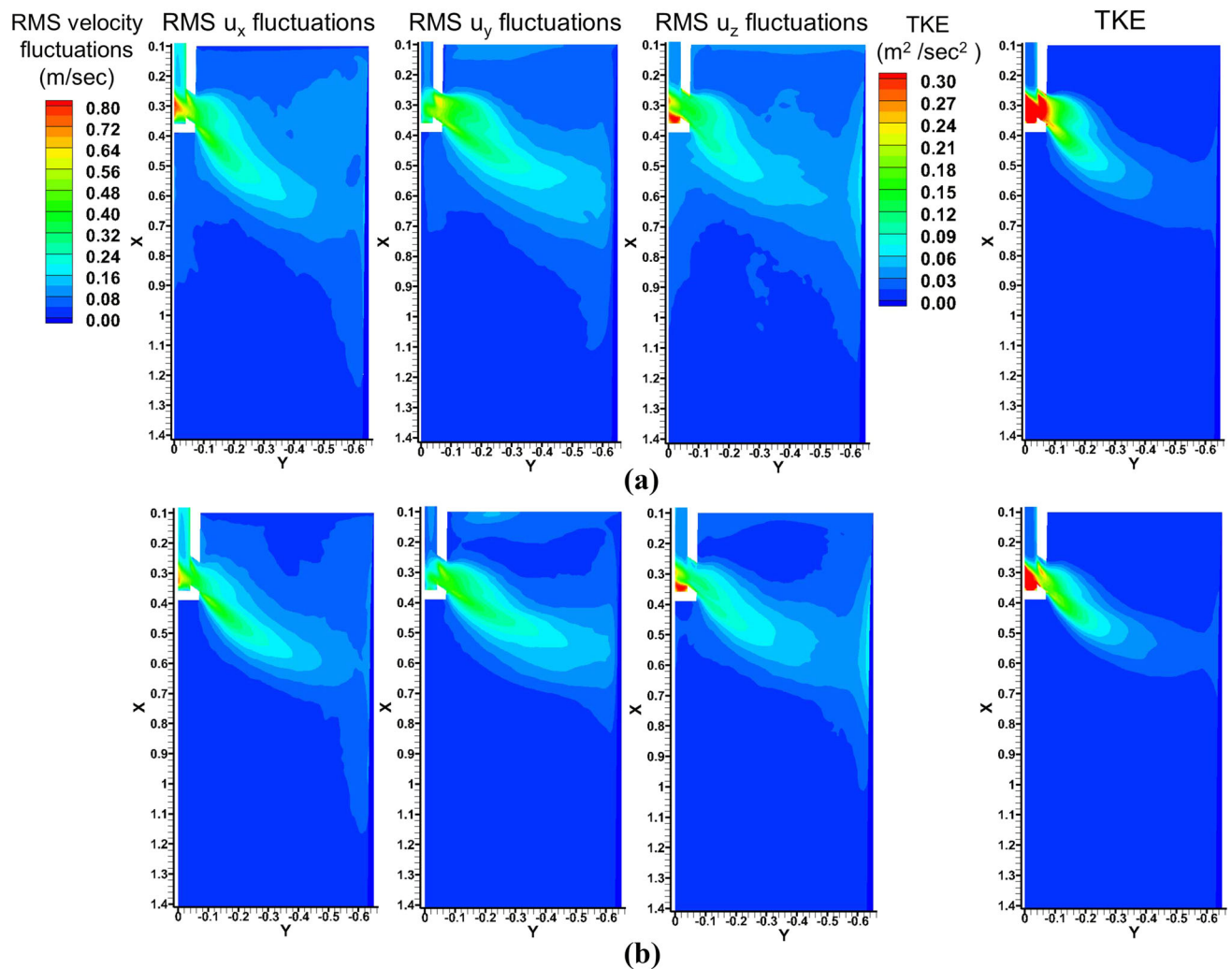


Fig. 8—Time-average RMS velocity component fluctuations and turbulent kinetic energy at the center-middle plane (between IR and OR) in the mold (a) without and (b) with EMBR.

slightly shallower average vertical jet angle, with smaller angle fluctuations. With a shallower impingement angle on the NF wall, stronger flow is sent up the NF after the jet splits. The slower jet flow with counter-clockwise swirl has less upward bending, and a deeper jet angle with more fluctuations, that sends weaker flow up the NF. As expected from the results of jet wobbling with EMBR, shown in Figure 7, vertical angle variations are reduced by ~ 30 pct: from 24.2 deg without EMBR, to 17.0 deg with EMBR, as given in Table IV.

Jet flow from clockwise nozzle swirl flow is directed slightly towards the OR, both with and without EMBR (2.7 and 1.6 deg horizontal angles). Because jet flow with clockwise swirl is more aligned to the mold center, the jet flow mainly impinges first on the NF, so retains more momentum to flow stronger up the NF. Jet flow with counter-clockwise swirl is directed strongly towards the IR (-5.6 deg horizontal angle), which may contribute to the steeper downward vertical angle. EMBR produces the same trends, but with less variations.

B. Surface Flow Variations

Transient flow through the SEN, nozzle port, and jet affects flow across the top surface at the interface with the slag layers, which is most relevant to steel quality. To investigate this surface flow, and more importantly, its time variations, time-averaged and instantaneous velocity contours with vectors are presented in Figure 12, at horizontal planes (30 and 400 mm below the surface) without EMBR. Example instantaneous snapshots of the flow pattern during times of clockwise and counter-clockwise nozzle swirl are shown at two cross sections, and are separated by the jet lag time of ~ 4.2 seconds. Although the time-averaged flow patterns are generally symmetric, these snapshots show asymmetric transient behavior with regions of high local velocity.

At 400 mm below the surface, the jet generally impinges first on the OR (with clockwise swirl) or IR (with counter-clockwise swirl) before reaching the NF. This jet flow phenomenon matches closely with previous observations in a water model with pulsed injection of

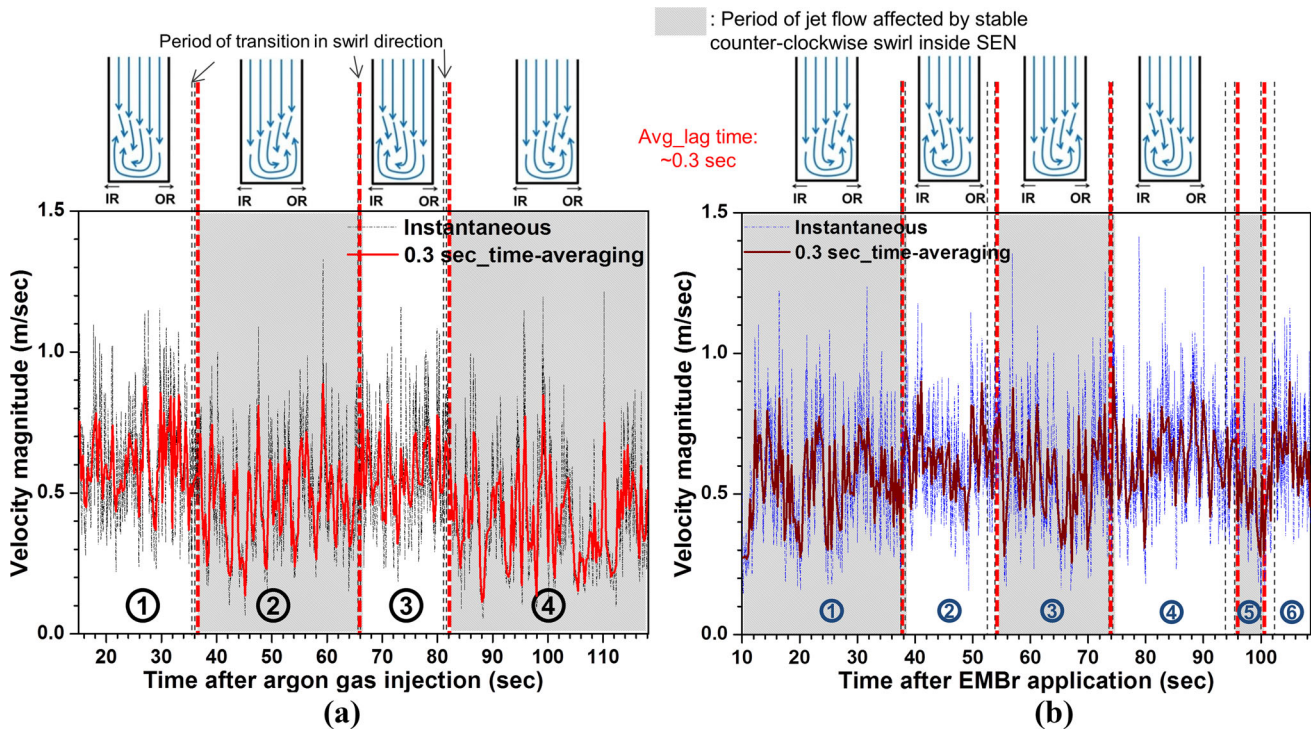


Fig. 9—Histories of jet flow velocity magnitude at P-2 (a) without and (b) with EMBR.

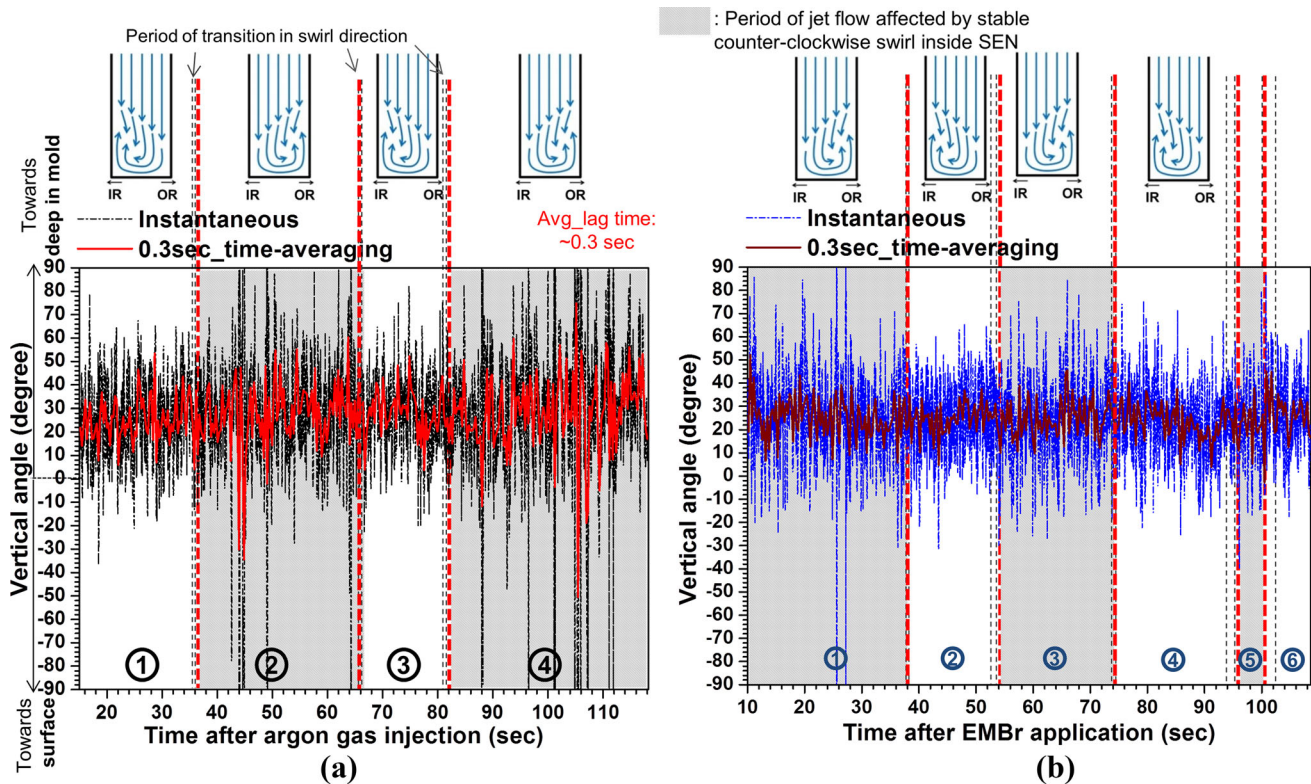


Fig. 10—Vertical angle histories of jet flow at P-2 (a) without and (b) with EMBR.

air bubbles.^[43] After reaching the NF, the jet flows upward towards the top surface, where biased cross flow is observed. The velocity and biased flow variations near

the top surface associated with changing swirl directions are quantified at point P-3 with time-averaged velocity magnitude and horizontal angle in Figures 13 and 14,

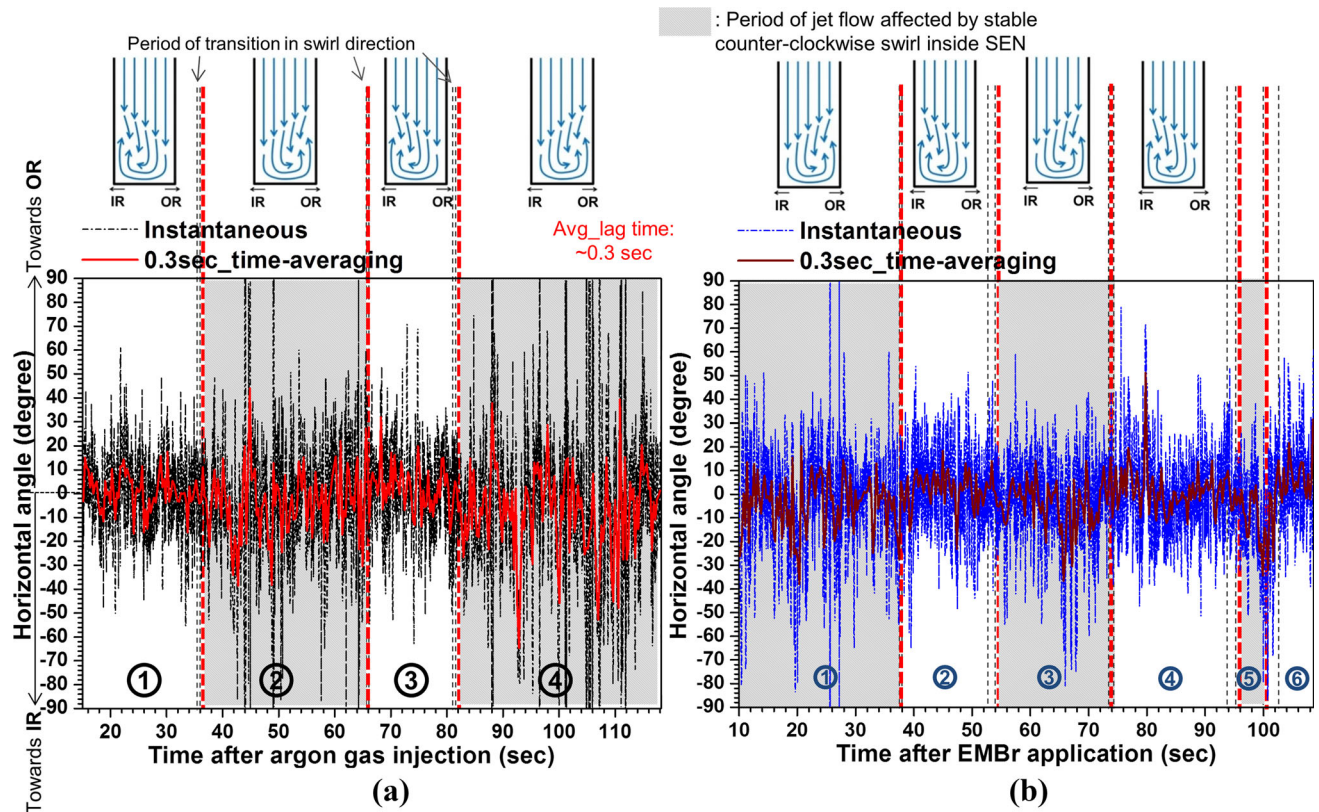


Fig. 11—Horizontal angle histories of jet flow at P-2 (a) without and (b) with EMBR.

respectively and in Table V. In these figures, red lines are drawn considering the average lag time (4.1 seconds without EMBR and 4.3 seconds with EMBR, from P-1 (nozzle port exit) to P-3) to show the time periods when surface flow is affected by stable counter-clockwise swirl.

Clockwise swirl leads to faster surface flow, as expected from the velocity magnitude histories at P-1 (at the nozzle port exit) and P-2 (inside jet in the mold). The increase is almost 50 pct, which reveals that the higher momentum of the clockwise swirling leaving the nozzle is magnified as it travels through the upper mold. Thus, swirl direction flipping in the nozzle is responsible for much of the variations in surface flow velocity. Specifically, the overall velocity variations of 0.073 m/s are ~40 pct larger than the variations of ~0.052 m/s during periods of stable swirl direction. Surface flow variations are less with EMBR, mainly due to the effect of the upper ruler magnetic field on flow near the top surface in the mold. Increased flow symmetry inside the SEN due to EMBR would be expected to be beneficial as well.

Biased flow (cross flow from OR to IR) across the top surface in the mold also is influenced by swirl direction in the nozzle, as indicated by the horizontal angle histories in Figure 14 and Table V. Clockwise swirl in the nozzle leads to biased cross flow usually towards the IR, with large angle fluctuations. Counter-clockwise swirl produces ~2X more asymmetric flow (but towards

the OR) with large increase in angle fluctuations. With EMBR, the angle fluctuations (biased flow) are greatly reduced, which agrees with previous work.^[44]

VI. ARGON BUBBLE DISTRIBUTION IN THE MOLD

The injection of ~1 million argon gas bubbles through the UTN refractory every 1 second causes over 6 million bubbles to accumulate and reside in the domain (including the nozzle, mold, and strand regions) once the mold flow pattern is fully developed in both the upper and lower rolls after ~100 seconds. Transient jet wobbling affected by swirl flipping also affects variations of the argon gas distribution in the mold, as shown in Figure 15. Strong jet flow with clockwise swirl causes more bubbles to follow the jet flow path into the upper mold region towards the NF. However, many bubbles float upward near the SEN walls, especially with EMBR. The larger backflow zone in the nozzle port with EMBR, likely enables more gas bubbles to collect there, and periodically suddenly release towards the top surface near the SEN. This could increase surface instability near the SEN and induce slag entrainment, which needs further work to investigate.

Without EMBR, most argon bubbles flow in the upper recirculation region and escape from the top surface. On

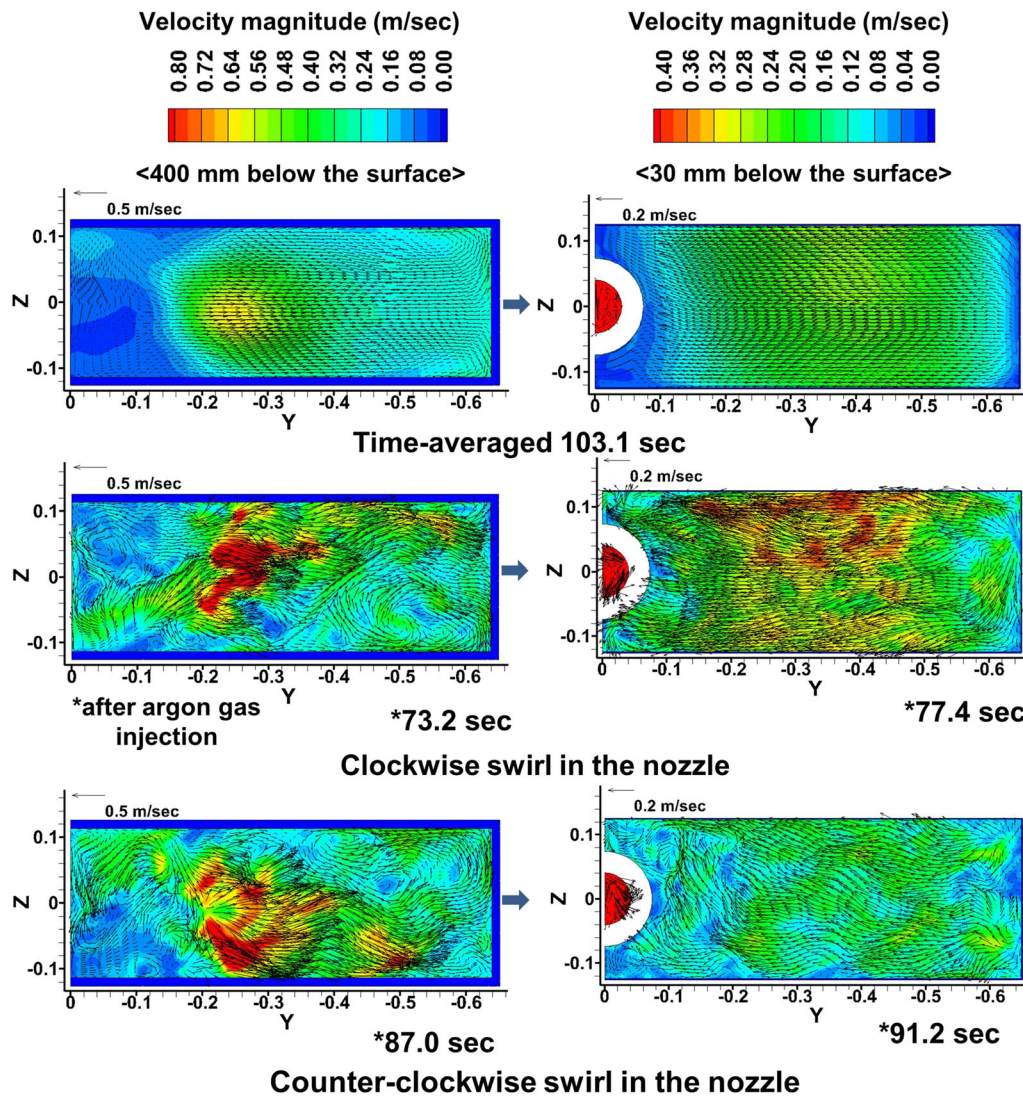


Fig. 12—Time-averaged and instantaneous velocity magnitude in jet flow region and at surface in the mold without EMBR.

the other hand, with EMBR, a significant amount of argon bubbles accompanies the stronger jet down the NF into the lower recirculation region, penetrating to 1100 mm below the top surface. In addition, the tight recirculation flow just below the jet, shown in Figure 7, gives the bubbles longer residence time near the NF with EMBR, and could increase bubble entrapment deep in the mold cavity. This somewhat detrimental effect of this particular EMBR configuration is due to the decrease in the field strength of the lower ruler towards the NF, as noted in previous work.^[31]

VII. MODEL VALIDATION

The two-phase LES models to predict molten steel-argon bubble flow with and without EMBR are validated by comparing the predicted surface velocity and surface level with measurements^[31] using nail board dipping tests and eddy-current sensor monitoring which were

performed in this caster in previous work, for the same casting conditions as used in the current study.

A. Surface Velocity

Time-averaged and instantaneous profiles of surface velocity magnitude predicted by the LES models, are compared with nail board measurements in Figure 16, with and without EMBR. Each line shows surface velocity magnitude profiles across the mold width at a cross-sectional center plane 10 mm below the interface between the molten steel and liquid mold flux layers. Symbols with error bars present time averages and standard deviations of ten dipping results at each measurement location. Details of these nail board dipping tests were given previously.^[32]

The model predicts both time and spatial variations of velocity magnitude near the surface, ranging from 0.04 to 0.44 m/s with and without EMBR. These variations associated with anisotropic turbulence are mainly due to flipping between clockwise and counter-clockwise swirl

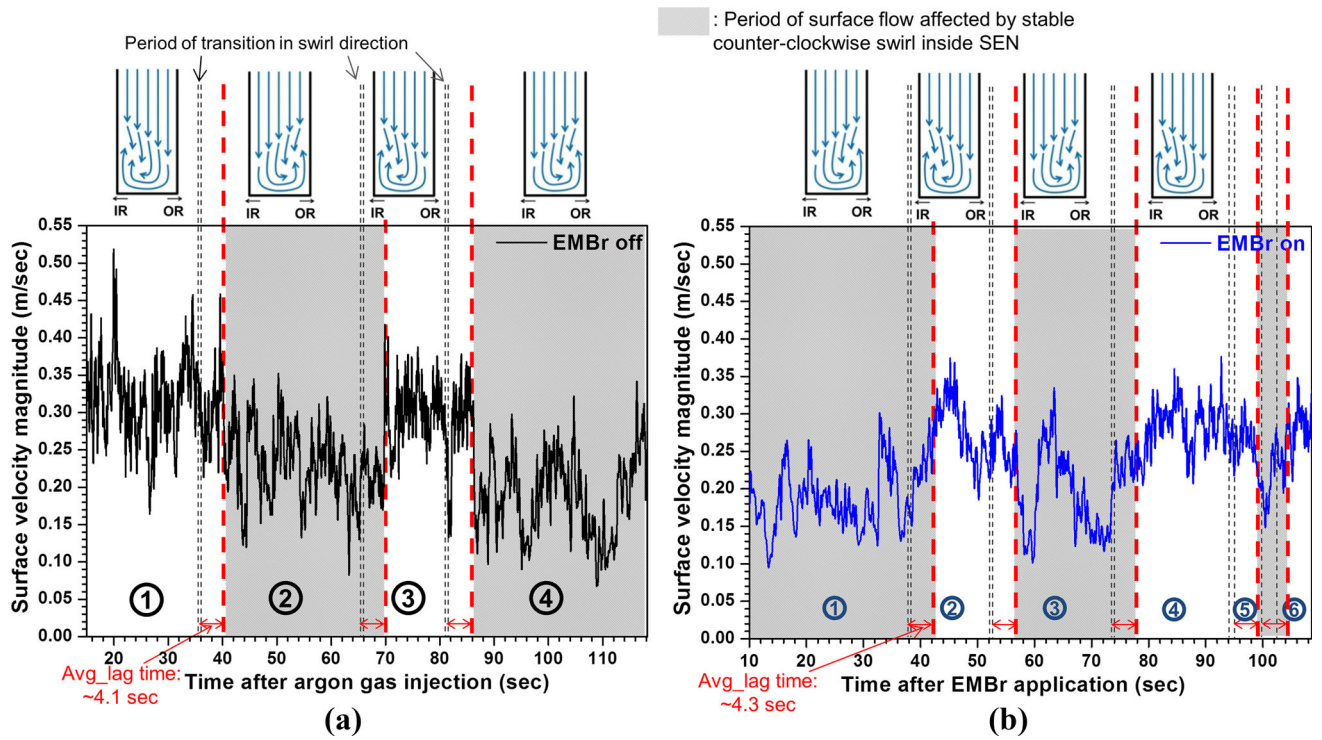


Fig. 13—Velocity magnitude histories at P-3 (surface) in the mold (a) without and (b) with EMBR.

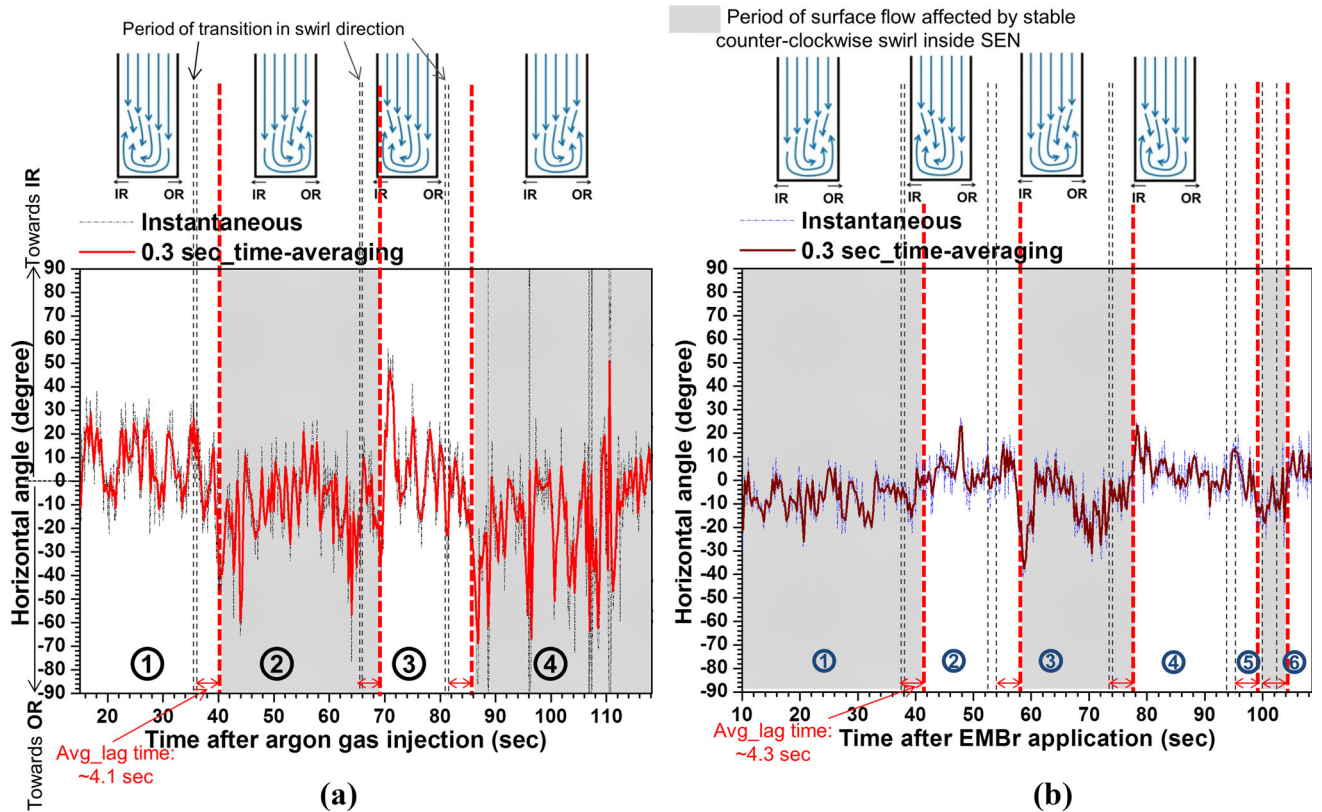


Fig. 14—Histories of horizontal angle of flow at P-3 (surface) (a) without and (b) with EMBR.

Table V. Flow Characteristics at P-3 (30 mm below the Surface) in the Mold

	Clockwise	Counter-clockwise	Total Time
Without EMBr			
Velocity magnitude	0.31 ± 0.052 m/s	0.21 ± 0.055 m/s	0.25 ± 0.073 m/s
Horizontal angle	6.16 ± 15.00 deg	-13.74 ± 23.38 deg	-6.15 ± 22.65 deg
With EMBr			
Velocity magnitude	0.28 ± 0.034 m/s	0.19 ± 0.046 m/s	0.23 ± 0.058 m/s
Horizontal angle	3.60 ± 7.29 deg	-7.83 ± 9.21 deg	-3.08 ± 10.36 deg

in the slide-gate nozzle. The surface velocity varies in all surface regions and is reduced with EMBr. For both cases with and without EMBr, the LES model shows remarkable agreement with the measurements. The qualitative and quantitative agreement of the time-averaged and range of instantaneous surface velocity magnitude profiles confirm that the LES model is an accurate tool to predict complex mold flow phenomena including multiphase effects and EMBr.

B. Surface Level

The surface-level height profile is calculated from the predicted static pressure distribution along the mold width at the mold surface as:

$$H_{i,t} = \frac{P_{i,t} - P_{\text{avg},t}}{[\rho_{\text{steel}} - (1 - c) \rho_{\text{slag}}]g}, \quad [7]$$

where $H_{i,t}$ is the surface-level height at location i and time t , $P_{i,t}$ is the static pressure at location i and time t , $P_{\text{avg},t}$ is the spatial-averaged pressure across the mold surface width at time t , ρ_{steel} is molten steel density, ρ_{slag} is slag density, and c is an empirical coefficient to consider the effect of slag displacement due to density differences on motion of the slag/molten steel interface. This was obtained from a linear trend analysis relating measured liquid slag height and measured molten steel height from the nail board tests.^[31] As given in Table VI, the coefficients are divided into three regions across the mold width.

As shown in Figure 17, the predicted time-average and instantaneous surface-level profiles agree reasonably well with the plant measurements, and their variations, both with and without EMBr. Counter-clockwise swirl in the nozzle produces flatter surface-level profiles along the mold width. Clockwise nozzle swirl produces high peaks near the NF, and the height difference across the width is much larger (~9 mm with clockwise; ~2 mm with counter-clockwise). Thus, level sloshing is observed due to flipping of the swirl direction. This sloshing is reduced with EMBr, which shows smaller variations between the level profiles. The measured variations of the level profiles are larger than the predictions, especially near the SEN. This is likely because the measurements cover 9 minutes but the predictions only cover ~100 seconds. During ~100 seconds, the LES model can capture only the high-frequency and low-amplitude components of the surface fluctuations. The low-frequency and high-amplitude wave motions observed in the measurements would

require much longer modeling time. Furthermore, the half domain for the modeling is unable to capture surface-level fluctuations caused by side-to-side sloshing between NFs. Thus, consideration of the full domain covering two NFs and a longer flow time are needed.

Figure 18 shows instantaneous and 1-second moving time-averaged surface levels at P-4 (the quarter point located midway between the SEN and the NF). Both the LES model predictions and the eddy-current measurements are compared with and without EMBr. Instantaneous surface-level fluctuations, $H_{\text{fluctuations}}$ from the model results are calculated as follows.

$$H_{\text{fluctuations}} = H_{i,t} - \frac{1}{n} \sum_{t=0}^n H_{i,t}, \quad [8]$$

where location i is the quarter point, t is the time step, n is the total number of time steps in the model run. The eddy-current sensor measurements over the quarter point were extracted from Figure 12(a) of Reference 31. The sensor had a 1-second response time.^[32] The model predictions with the 1-second moving time average show reasonable agreement with this measured signal.

VIII. SUMMARY AND CONCLUSIONS

This work applied an LES model of the slide gate, nozzle, and mold, during nominally steady continuous casting of steel slabs to gain insights into nozzle swirl, jet wobbling, and surface flow variations of transient flow of molten steel and argon gas, with and without electromagnetic forces. The model included a coupled Lagrangian DPM for argon gas injection, and the magnetic induction MHD model for double-ruler EMBr. Analysis of two simulations of ~100 seconds each reveal:

1. The asymmetrically positioned slide-gate middle plate, with its open area near the outside radius side, sends much stronger flow down the OR side of the nozzle. This flow most often (63.9 pct of the time without EMBr, 53.0 pct of the time with EMBr), crosses over to send stronger flow into the nozzle port region down the opposite (IR) side of the nozzle.
2. When flow is predominantly down the OR side, the velocity is higher and clockwise swirl is produced in the nozzle bottom, with stronger jet velocity exiting the nozzle.

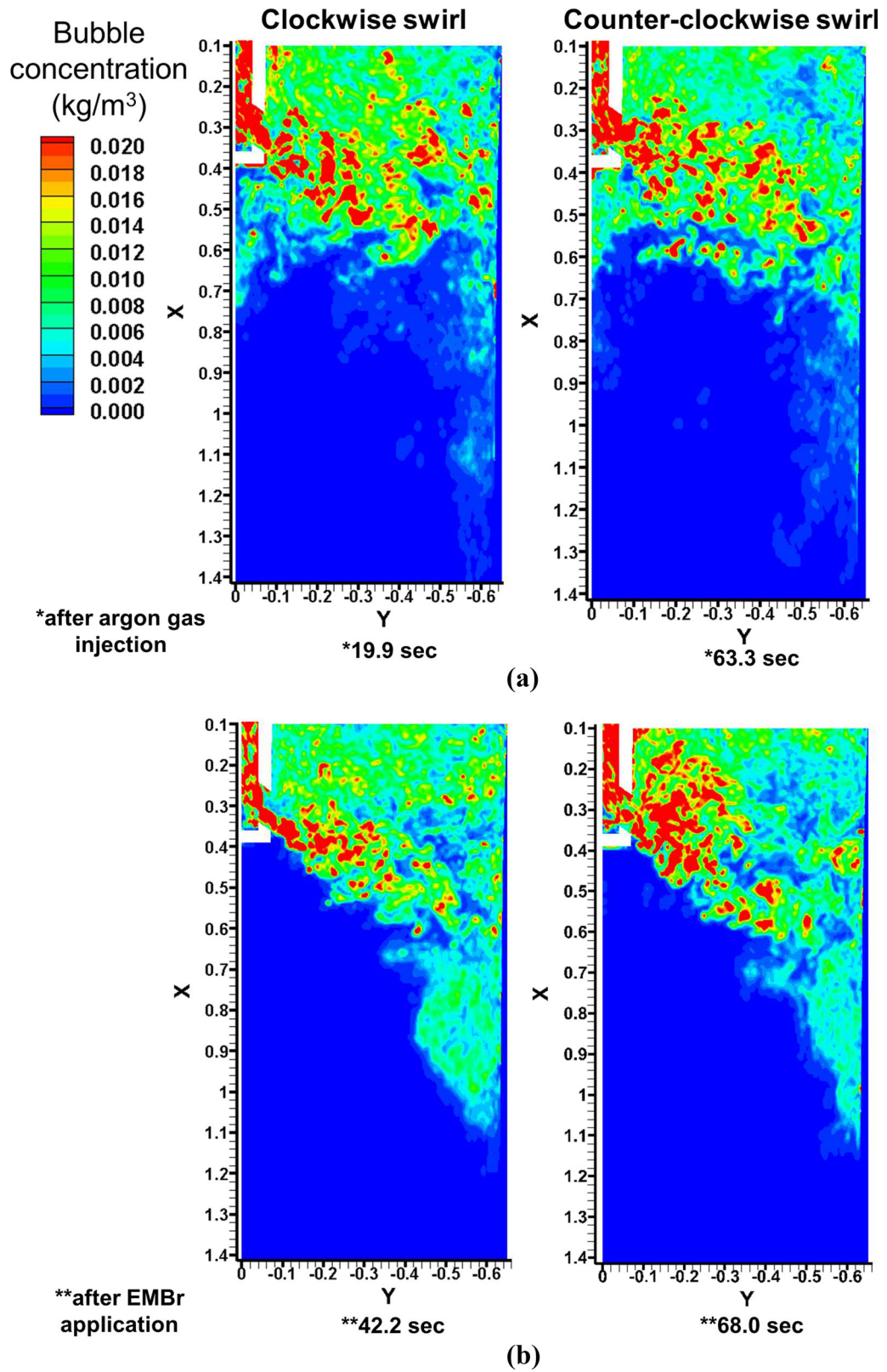


Fig. 15—Argon bubble distribution in the mold (a) without and (b) with EMBR.

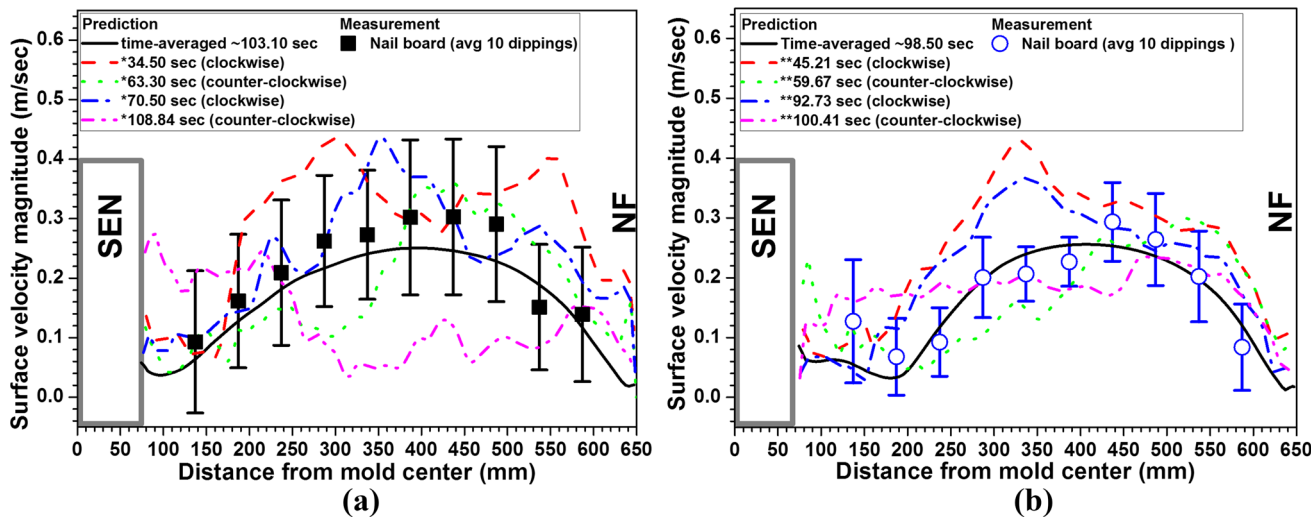


Fig. 16—Comparison of surface velocity magnitude between the LES prediction and the nail board measurements (a) without and (b) with EMBR.

Table VI. Coefficient of Slag Motion at the Surface in the Mold with and Without EMBR^[31]

	SEN Region 1 (135 to 235 mm from Mold Center)	Quarter-Point Region 2 (235 to 485 mm from Mold Center)	Narrow Face Region 3 (485 to 585 mm from Mold Center)
Without EMBR	0.85	0.74	0.82
With EMBR	0.97	0.63	0.65

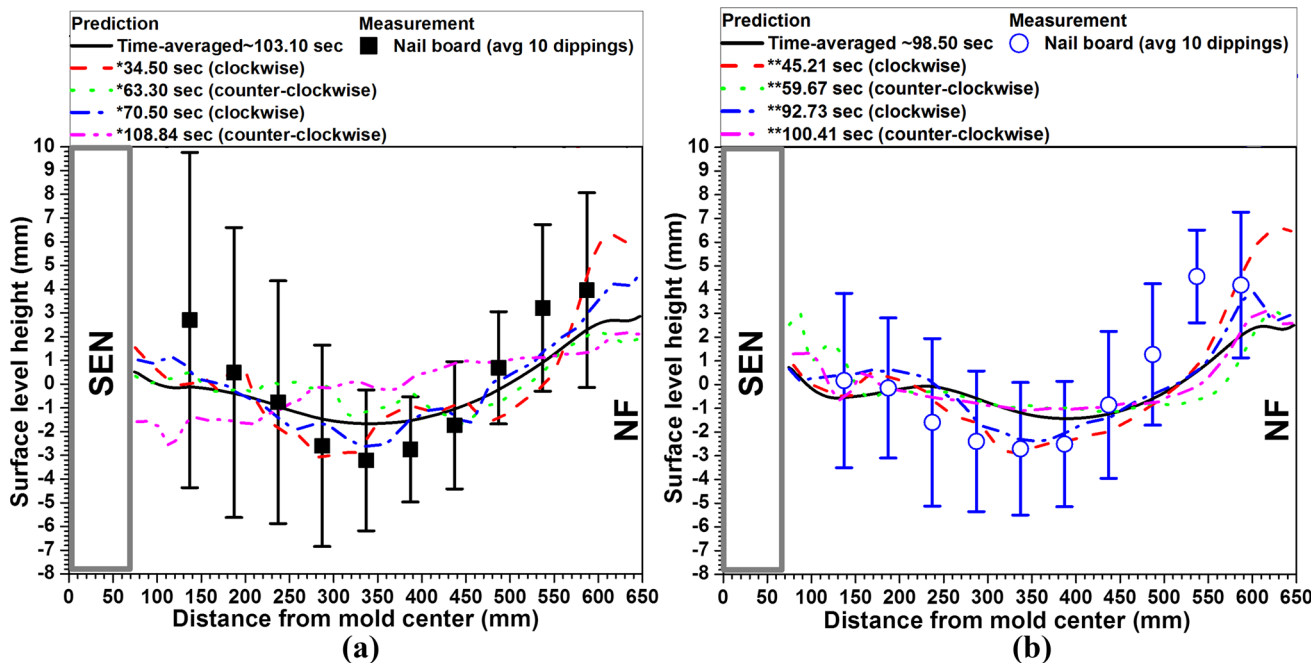


Fig. 17—Comparison of surface-level variations between the LES prediction and the nail board measurements (a) without and (b) with EMBR.

3. Transient flow in the well-bottom region is almost always swirling (over 93 pct of the time), alternating chaotically between clockwise and counter-clockwise rotation, persisting for 5 to 30 seconds time intervals

before flipping directions every 0.6 to 2.3 seconds. The counter-clockwise swirl direction was slightly more predominant, as expected because it is produced by the stronger flow down the opposite side of the nozzle.

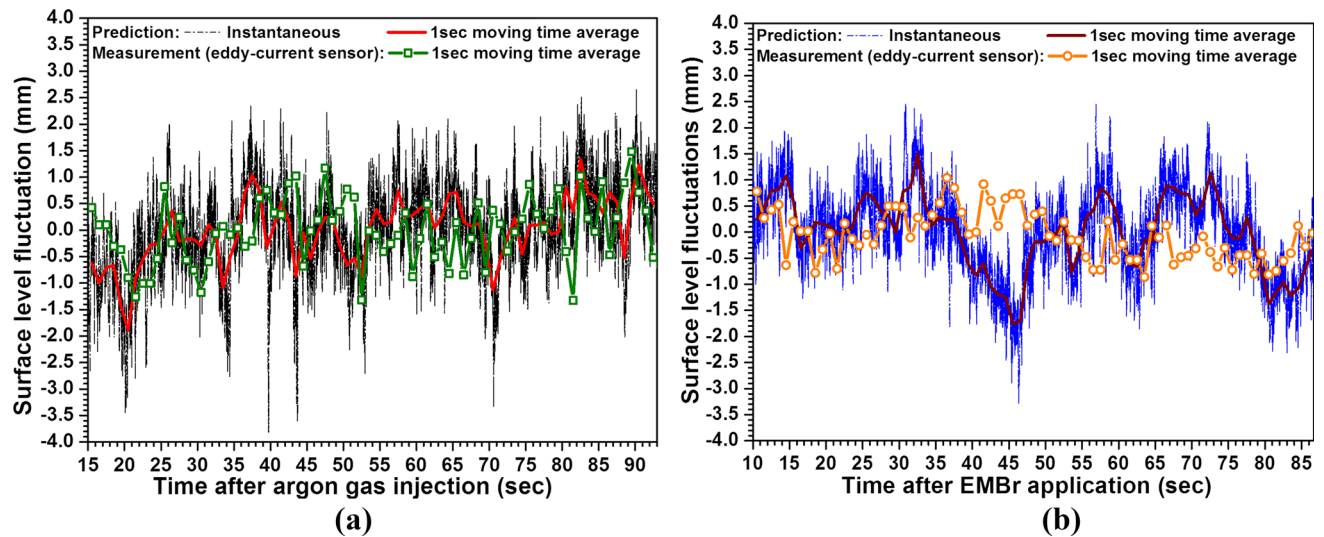


Fig. 18—Surface-level histories at quarter-point P-4 (a) without and (b) with EMBr.

4. Counter-clockwise swirl in the nozzle produces a lower average velocity at port exit, with slightly larger fluctuations, relative to clockwise swirl. This is likely due to the longer path from the middle plate to the well bottom lowering the flow momentum. When the swirl direction is clockwise, higher average velocity is produced because the higher flow straight down the OR side has higher momentum owing to the shorter, more direct path.
5. Transient jet flow from the nozzle port to the mold shows both up-and-down and IR-OR wobbling with accompanying time variations of velocity, horizontal angle, and vertical angle.
6. Counter-clockwise nozzle swirl produces jet flow that is ~ 37 pct slower (without EMBr) and ~ 17 pct slower (with EMBr). The faster jet flow with clockwise swirl impinges more towards the OR with a shallower vertical jet angle (bending more upward towards the top surface), and causes faster surface flow with smaller flow angle variations.
7. The double-ruler EMBr in the current work creates two regions having equally strong magnetic field peaks (~ 0.17 T) across the mold width: one centered just above the port (~ 250 mm below the mold top) and the other centered farther below the nozzle port (~ 750 mm below the mold top). Both peaks in the field significantly decrease in strength towards the NF.
8. Swirl direction flipping occurs more frequently with EMBr than without EMBr; The EMBr reduces the flow asymmetries and decreases the turbulence produced by the jet wobbling, resulting in a thinner time-averaged jet, with smaller velocity fluctuations.
9. Velocity variations and flow angle variations at the top surface, produced by the nozzle swirl direction flipping, are decreased by imposing the EMBr.
10. The transient surface velocity and surface-level predictions from the LES model coupled with Lagrangian DPM match well with both the time averages and variations measured with the nail

board dipping tests and the eddy-current level sensor, both with and without EMBr. Longer simulations with a full domain are needed to capture the important low-frequency, high-amplitude variations.

ACKNOWLEDGMENTS

The authors thank POSCO for their assistance in collecting plant data and financial support (Grant No. 4.0004977.01), and Mr. Yong-Jin Kim, POSCO for help with the plant measurements. Support from the National Science Foundation (Grant No. CMMI 11-30882) and the Continuous Casting Consortium, University of Illinois at Urbana-Champaign, USA is gratefully acknowledged. This research is also part of the Blue Waters sustained petascale computing project at the National Center for Supercomputing Applications at the University of Illinois, which is supported by the National Science Foundation (Awards OCI-0725070 and ACI-1238993) and the State of Illinois.

REFERENCES

1. C. Ojeda, B.G. Thomas, J. Barco and J.L. Arana: *Proc. of AIS-Tech 2007*, Assoc. Iron Steel Technology, Warrendale, PA, 2007, pp. 269–83.
2. J. Sengupta, C. Ojeda, and B.G. Thomas: *Int. J. Cast Met. Res.*, 2009, vol. 22, pp. 8–14.
3. M. Iguchi, J. Yoshida, T. Shimizu, and Y. Mizuno: *ISIJ Int.*, 2000, vol. 40, pp. 685–91.
4. L.C. Hibbeler, R. Liu, and B.G. Thomas: *Proc. of 7th ECCO*, Steel Institute VDEh, Germany, 2011, pp. 1–10.
5. R. Hagemann, R. Schwarze, H.P. Heller, and P.R. Scheller: *Metall. Mater. Trans B*, 2013, vol. 44B, pp. 80–90.
6. S.-M. Cho, G.-G. Lee, S.-H. Kim, R. Chaudhary, O.-D. Kwon, and B. Thomas: *Proc. of TMS 2010*, TMS, Warrendale, PA, USA, 2010, pp. 71–77.
7. S.-M. Cho, S.-H. Kim, R. Chaudhary, B.G. Thomas, H.-J. Shin, W.-R. Choi, and S.-K. Kim: *Iron Steel Technol*, 2012, vol. 9, pp. 85–95.

8. H. Bai and B.G. Thomas: *Metall. Mater. Trans. B*, 2001, vol. 32B, pp. 269–84.
9. T. Shi: Master degree thesis, University of Illinois at Urbana-Champaign, 2001.
10. H. Bai and B.G. Thomas: *Metall. Mater. Trans. B*, 2001, vol. 32B, pp. 269–84.
11. Y. Miki and S. Takeuchi: *ISIJ Int.*, 2003, vol. 43, pp. 1548–55.
12. Z.-Q. Liu, B.-K. Li, M.-F. Jiang, and F. Tsukihashi: *ISIJ Int.*, 2013, vol. 53, pp. 484–92.
13. K. Takatani, K. Nakai, T. Watanabe, and H. Nakajima: *ISIJ Int.*, 1989, vol. 29, pp. 1063–68.
14. H. Harada, T. Toh, T. Ishii, K. Kaneko, and E. Takeuchi: *ISIJ Int.*, 2001, vol. 41, pp. 1236–44.
15. Z.-D. Qian and Y.-L. Wu: *ISIJ Int.*, 2004, vol. 44, pp. 100–107.
16. K. Cukierski and B.G. Thomas: *Metall. Mater. Trans. B*, 2008, vol. 39B, pp. 94–107.
17. K. Timmel, S. Eckert, G. Gerbeth, F. Stefani, and T. Wondrak: *ISIJ Int.*, 2010, vol. 50, pp. 1134–41.
18. K. Timmel, S. Eckert, and G. Gerbeth: *Metall. Mater. Trans. B*, 2011, vol. 42B, pp. 68–80.
19. X. Miao, K. Timmel, D. Lucas, Z. Ren, S. Eckert G. Gerbeth: *Metall. Mater. Trans. B*, 2012, vol. 43B, pp. 954–72.
20. R. Chaudhary, B.G. Thomas, and S.P. Vanka: *Metall. Mater. Trans. B*, 2012, vol. 43B, pp. 532–53.
21. R. Singh, B.G. Thomas, and S.P. Vanka: *Metall. Mater. Trans. B*, 2013, vol. 44B, pp. 1201–21.
22. R. Singh, B.G. Thomas, and S.P. Vanka: *Metall. Mater. Trans. B*, 2014, vol. 45B, pp. 1098–1115.
23. B. Li, T. Okane, and T. Umeda: *Metall. Mater. Trans. B*, 2000, vol. 31B, pp. 1491–1503.
24. B. Li, T. Okane, and T. Umeda: *Metall. Mater. Trans. B*, 2001, vol. 32B, pp. 1053–66.
25. Y. Wang and L. Zhang: *Metall. Mater. Trans. B*, 2011, vol. 42B, pp. 1319–51.
26. H. Yu and M. Zhu: *ISIJ Int.*, 2008, vol. 48, pp. 584–91.
27. B. Li and F. Tsukihashi: *ISIJ Int.*, 2003, vol. 43, pp. 923–31.
28. K. Moon, H. Shin, B. Kim, J. Chung, Y. Hwang, and J. Yoon: *ISIJ Int.*, 1996, vol. 36, pp. S201–203.
29. Y. Hwang, P. Cha, H. Nam, K. Moon, and J. Yoon: *ISIJ Int.*, 1997, vol. 37, pp. 659–67.
30. S.-M. Cho, H.-J. Lee, S.-H. Kim, R. Chaudhary, B. G. Thomas, D.-H. Lee, Y.-J. Kim, W.-R. Choi, S.-K. Kim, and H.-S. Kim: *Proc. Of. TMS 2011*, TMS, Warrendale, PA, 2011, pp. 59–66.
31. S.-M. Cho, S.-H. Kim, and B.G. Thomas: *ISIJ Int.*, 2014, vol. 54, pp. 855–64.
32. S.-M. Cho, S.-H. Kim, and B.G. Thomas: *ISIJ Int.*, 2014, vol. 54, pp. 845–54.
33. ANSYS FLUENT 14.5-Theory Guide, *ANSYS. Inc.*, Canonsburg, PA, USA, 2012.
34. Q. Yuan: Ph. D. Thesis, University of Illinois at Urbana-Champaign, 2004.
35. Q. Yuan, B.G. Thomas, and S.P. Vanka: *Metall. Mater. Trans. B*, 2004, vol. 35B, pp. 685–702.
36. R. Liu: Ph. D. Thesis, University of Illinois at Urbana-Champaign, 2015.
37. F. Nicoud and F. Ducros: *Flow, Turb. Comb.*, 1999, vol. 63(3), pp. 183–200.
38. ANSYS FLUENT 14.5-Magnetohydrodynamics (MHD) Module Manual, *ANSYS. Inc.*, Canonburg, PA, USA, 2012.
39. H. Bai and B.G. Thomas: *Metall. Mater. Trans. B*, 2001, vol. 32B, pp. 1143–59.
40. G.-G. Lee, B. G. Thomas, and S-H Kim: *Met., Mater. Int.*, 2010, vol. 16, pp. 501.
41. D.E. Hershey, B.G. Thomas, and F.M. Najjar: *Int. J. Numer. Methods. Fluids*, 1993, vol. 17, pp. 23–47.
42. M. Schmitz and M. Byrne: Bethlehem Steel, Sparrows Point, Baltimore, private communication, 1992.
43. D. Gupta and A.K. Lahiri: *Metall. Mater. Trans. B*, 1996, vol. 27B, pp. 757–64.
44. K. Jin, S. P. Vanka, B. G. Thomas, and X. M. Ruan: *Proc. Of. TMS 2016*, TMS, Nashville, 2016, pp. 159–66.